RSC Advances

ROYAL SOCIETY OF CHEMISTRY

www.rsc.org/advances

Gold nanoparticle incorporation into nanoporous anatase TiO_2 Mesocrystal using a simple deposition-precipitation method for photocatalytic applications

Tiehu Han, Huigang Wang*, Xuming Zheng*

Department of Chemistry, Engineering Research Center for Eco-dyeing and Finishing of Textiles, MOE and Zhejiang Provincial Top Key Academic Discipline of Chemical Engineering and Technology, *Zhejiang Sci-Tech University, Hangzhou 310018, China*

CORRESPONDING AUTHOR FOOTNOTE

Professor Ph.D. Huigang Wang
Email: zdwhg@163.com, huigwang@uni-osnabrueck.de
Department of Chemistry Phone: 00186-571-8684-3627
Zhejiang Sci-Tech University
Hangzhou, 310018
China

Abstract: Spindle-shaped nanoporous anatase TiO_2 mesocrystals with exposed active {101} facets have been successfully prepared through a hydrothermal method with the tetrabutyltitanateas as the precursor. By deposition-precipitation process, highly dispersed Au nanoparticles loaded on spindle-shaped MesoTiO_2 exposed {101} facets, denoted as Au_x/MesoTiO_2, were firstly fabricated to establish close Schottky junctions to improve the visible light activity and the stability of Au on the catalyst surface. The photo degradation of methylene blue (MB) over Au_x/MesoTiO_2 was systematically investigated. The exposed active {101} facets together with the loaded Au nanoparticles dramatically enhanced the visible light photocatalytic activity of the TiO_2. Synergistic effect of the high intrinsic single-crystal-like nature, the stability of the gold and the strong interaction between the Au and MesoTiO_2 make the catalysis exhibit extraordinary photocatalytic stability. The detailed e^- and h^+ separation dynamics for visible-light and UV-Vis induced catalytic mechanism was discussed.

Keywords Au_x/TiO_2 mesocrystals; Spindle-shaped; Schottky junctions; visible light photocatalysis; Plasmon resonance

1. Introduction

In response to the increasing environmental and energy related concerns, photocatalysis using sunlight have been attracting tremendous attention[1, 2]. Among the variety of photocatalysts, titania (TiO_2) has proven to be the most widely used photocatalyst in applications such as environmental cleaning and hydrogen energy[3, 4]. However, TiO_2 is far from being a perfect photocatalyst due to its wide bandgap which limits its photo-absorption to the UV region (about 5% of solar light). In order to extend the photoresponse from UV to visible light region, great efforts have been made to modify TiO_2 such as doping[5, 6], metal deposition[7-9], surface sensitization[10-12] and coupling of composite semiconductors[13-15].

As a novel class of TiO_2 material, TiO_2 mesocrystal has received rapidly increasing attention since anatase TiO_2 mesocrystals (MesoTiO_2) were first prepared by topotactic conversion from NH_4TiOF_3 mesocrystals in the presence of nonionic surfactants[16, 17]. Bian and co-workers reported that the MesoTiO_2 superstructures significantly enhance the charge separation upon UV-light irradiation due to the remarkably long-lived charges[18]. Hong and co-workers reported an experimental study of a new synthesis strategy for the formation of unique rutile TiO_2 mesocrystals constructed from ultrathin nanowires in the absence of an additive. The rutile TiO_2 mesocrystals were used for the first time as the electrode in LIBS and exhibited a large reversible lithium-ion charge-discharge capacity and excellent cyclic stability[19]. However, it remains a great challenge to transfer mesocrystals into applications because of poor understanding of their formation processes.

Recently, Au/TiO_2, the representative of "plasmonic photocatalyst", has attracted much interest as a new type of visible light photocatalyts[20-23]. Gold is a noble metal and does not undergo corrosion under photocatalytic conditions. In the photocatalytic process, the noble metal plays an important role: on one hand, due to the surface plasmon resonance (SPR), gold nanoparticles (NPs) possess unique absorption in the whole visible region, which can be utilized to harvest the visible light[20-23]; on the other hand, the formation of Schottky barrier between TiO_2 and

Au NPs is help to inhibit the e-h pairs recombination process[24]. The photocatalytic reaction of Au/TiO_2 mainly occurs on the surface of TiO_2. The TiO_2 surface can transfer the electrons from its conduction band (CB) to Au[8] or accepts the electrons from Au[25, 26], which depends on whether the excitation occurs on TiO_2 or on the surface plasmon band of Au[25,27]. Automatically, how about the photocatalytic activity of the Meso TiO_2 after loading Au NPs under visible light irradiation? However, the incorporation of plasmonic Au NPs onto Meso TiO_2 has not been reported.

In this study, a simple deposition-precipitation (DP) method[28, 29] was used to deposit Au NPs on MesoTiO_2 which synthesized through a solvothermal method using tetrabutyltitanateas(TBT) as the titanium source and acetic acid as the solvent[30, 31]. The photocatalytic activity of Au/MesoTiO_2 samples under simultaneous UV and visible light irradiation or visible light irradiation alone was evaluated by the degradation capability of methylene blue (MB). Furthermore, we also carefully investigate the influences of Au content on the microstructures and photocatalytic activity of MosoTiO_2 samples. It was found that the superstructure-based Au/MesoTiO_2 with suitable gold content can significantly enhance the photocatalytic activity.

2. Experimental section

2.1 Synthesis of spindle-shaped nanoporous anatase TiO_2 mesocrystals

Spindle-shaped nanoporous anatase TiO_2 mesocrystals were synthesized by the solvothermal reaction of the TBT-HAc solution. In a typical synthesis, 1 mL of TBT was added dropwise to 50 mL of HAc with continuous stirring. The obtained white suspension was transferred to a dried Teflon autoclave with a capacity of 100 mL, and then kept at 200℃ for 24 h. After being cooled to room temperature, the product was collected by high-speed centrifugation, washed with ethanol several times, dried at 60 ℃ overnight, and finally calcined at 400 ℃ for 30 min to remove the residual organics.

2.2 Synthesis of Au/MesoTiO_2

Au/MesoTiO_2 catalysts were prepared by a deposition-precipitation (DP) method. In the standard preparation conditions, 100 mL of an appropriate concentration of hydrogen tetrachloroaurate(□) trihydrate ($HAuCl_4 \cdot 3H_2O$, Alfa Aesar, 99.99%) was heated to 80℃. 1 g of respective TiO_2 was dispersed in the solution, and the pH was readjusted to 8.0 with NaOH (1 M). The suspension was then stirred for another 4h at 80℃. After being cooled to room temperature, the product was centrifuged, washed and dried. Finally, the sample was calcined at 300 ℃ for 4 h to obtain the Au_x/MesoTiO_2, where x is the amount (in wt%) Au loaded[x%=Au/(Au+MesoTiO_2)× 100%].

2.3 Characterization

Crystalline phases of the prepared samples was characterized by X-ray diffraction (XRD) on a DX-2700 diffractometer (Dandong Hanyuan Instrument Co. Ltd, China) using Cu Ka radiation (λ = 0.15418 nm). Transmission electron microscope (TEM) images were taken on a JEOL-2100 electron microscope operating at an accelerating voltage of 200 kV. The morphology of materials was analyzed by a Hitachi S-4800 Field emission scanning electron microscope (FE-SEM). UV-vis diffuse-reflectance spectroscopy (DRS) was obtained from a Shimadzu UV-2450 spectrophotometer using $BaSO_4$ as the reference. The specific surface area of sample was deduced by the BET method (N_2 adsorption) with a Micromeritics ASAP 2020 system. X-ray photoelectron spectroscopy (XPS) was performed on a Kratos AXIS Ultra DLD

instrument with an AL Ka monochromatic source. All binding energies were referenced to the C1s peak (284.6 eV) arising from adventitious hydrocarbons. The 488-nm Raman measurements were carried out on the quartz cell with the use of an experimental apparatus consisting of a triplemonochromator (TriVista TR557, Princeton Instruments) equipped with an argon ion laser (Coherent, CVI MELLES GRIOT) as a source of exciting light at 488 nm (20 mW on the sample) and with a liquid-nitrogen-cooled charge coupled device (CCD) array (Princeton Instruments Inc.; model ID:LN/2048X512.B/I,UVAR.) allowing a wavenumber coverage of 1089 cm^{-1} within the chip active area and a spectral resolution (the instrumental apparatus function, full width at half maxima) of 2.5 cm^{-1}.

2.4 Photocatalysis Experiments

The photocatalytic activities of materials were examined by degrading methylene blue (MB) in aqueous under visible light irradiation using a 300 W Xenon lamp (CEL-HXUV300, Beijing CEAULIGHT) with a 400 nm cutoff filter as the light source. In each experiment, a total of 50 mg of catalyst was added to a 100 mL solution of 10 mg/L MB in a 120 mL quartz reactor with a circulating water system to maintain a constant temperature, and the distance between the light and the surface of the solution was set at about 10 cm. Before irradiation, the suspension was stirred in the dark for 30 min to make sure the adsorption-desorption equilibrium of solution. After the start of photocatalytic reaction, approximately 4 mL of the mixture was taken at regular time intervals, and then centrifuged to separate the photocatalyst particles. The concentration was analyzed by measuring the maximum absorbance at 665 nm for MB using a UV-vis spectrometer (Varian Cary 50).

3 Results and discussion

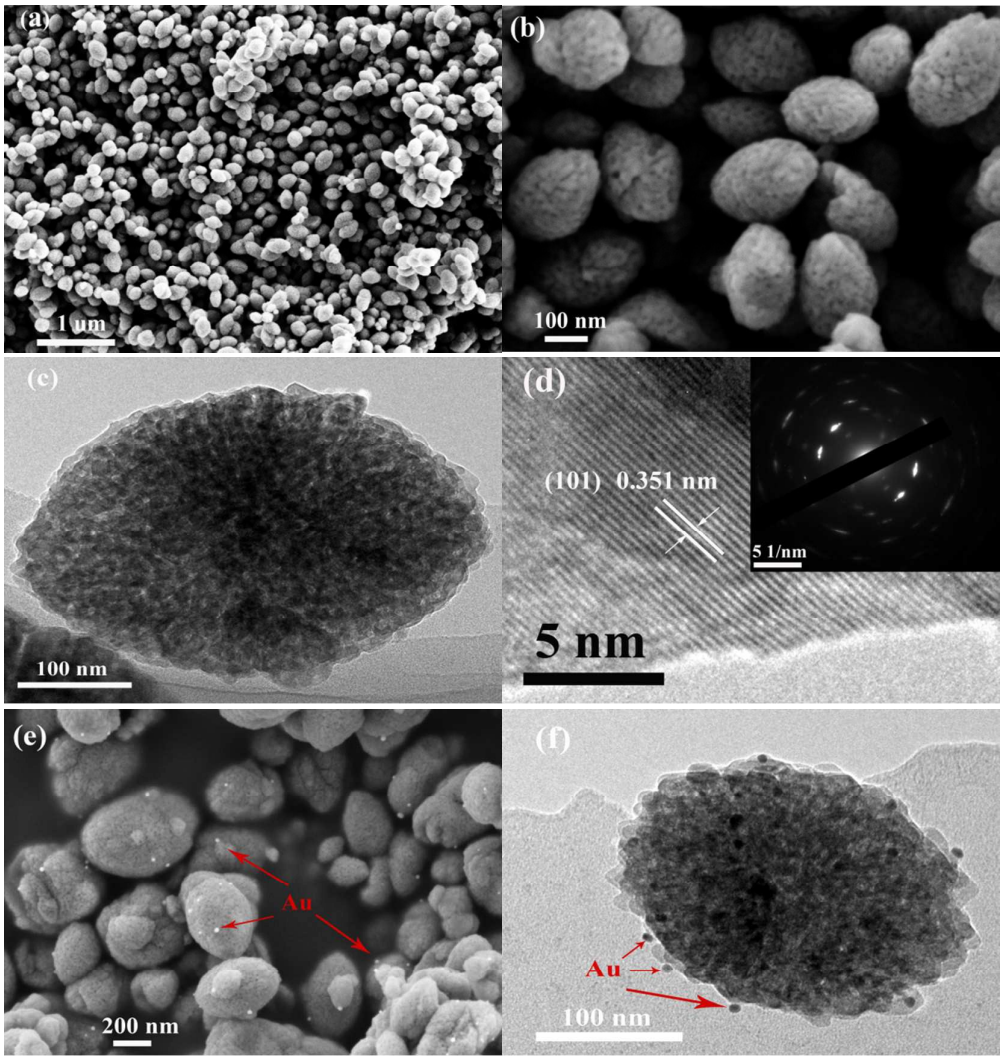

Fig.1FE-SEM images (a and b) and TEM image (c) of the MesoTiO$_2$. HRTEM image of the MesoTiO$_2$ (d) and selective area electron diffraction (SAED, inset d). FE-SEM and TEM images of the Au5.0/MesoTiO$_2$ (e and f).

Fig.1a,b shows the representative FE-SEM images of the synthesized MesoTiO$_2$. An overview image at low magnification (see Fig.1a) illustrates that a large quantity of particles have formed with uniform spindle shape and unique size. The lengths and diameters are mostly found to be 300-400nm and 200-300nm, respectively. A high-magnification SEM image shown in Fig.1b reveals that the spindle-shaped particles are composed of primary nanoparticles, which make their surface rough and porous. The latter was subsequently confirmed by the pore analysis based on N_2

adsorption measurements (discussed below). The TEM image in Fig.1c shows the unique MesoTiO$_2$, confirming that the particle consists of nanosized subunits. Both the HTTEM image (Fig.1d) and the selective area electron diffraction (SAED, inset of Fig.1d) show well resolved {101} lattice fringes (distance 0.352nm) and diffraction cycles indicative of a highly crystalline TiO$_2$ anatase framework. The dominant exposed face of the spindle-shaped nanoporous anatase TiO$_2$ mesocrystals is {101}. These exposed {101} facets were taken as an ideal support for highly dispersed Au nanoparticles to improve the stability of Au and visible light activity. It is clear to see that the diffraction spots are slightly elongated, indicating that a mesocrystal structure was formed[19, 32]. Fig.1e shows the typical SEM image of Au$_{5.0}$/MesoTiO$_2$. Well dispersed Au nanoparticles (bright dots) can be discerned from the background. It is evident that the DP process has affected the morphology and size of MesoTiO$_2$ in this study. The TEM image of an individual particle of Au$_{5.0}$/MesoTiO$_2$ (Fig.1f) indicates that the Au NPs are nearly spherical with an average size of about 8 nm. Additional XPS results confirmed that the deposited Au NPs were metallic Au(0) in Au/MesoTiO$_2$ samples (discussed below).

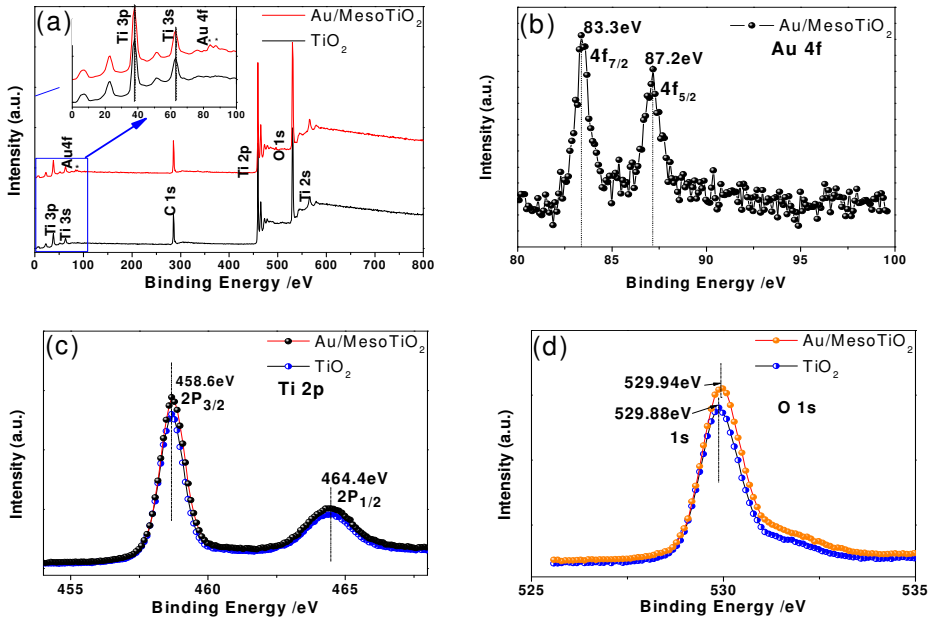

Fig.2(a) Wide-scan XPS survey spectra for the MesoTiO$_2$ before and after Au loading. (b) Au4f XPS spectra from Au$_{5.0}$/MesoTiO$_2$. The inset of (a) is the corresponding

amplification image of (a). High-resolution XPS spectra of (c) Ti2p and (d) O1s forthe $MesoTiO_2$ before and after Au loading.

To investigate the surface composition and the chemical states of the elements in as-prepared $Au/MesoTiO_2$, XPS studies were conducted over $MesoTiO_2$ before and after Au loading. As shown in Fig.2a, the wide-scan survey spectra of $MesoTiO_2$ and $Au/MesoTiO_2$ all contains O, Ti and C elements, the emergence of the C element can attribute to the residual carbon from the sample and adventitious hydrocarbon from XPS instrument itself. The inset in (a) shows the spectra comparison between $MesoTiO_2$ and $Au/MesoTiO_2$ in the range of 0-100 eV, obviously there are some weak peaks in the range of 80-100 eV for $Au/MesoTiO_2$ which can be ascribed to the Au4f. the Au4f core level spectrum, shown in Fig.2b, is composed of two peaks at the binding energies of 83.3 and 87.2 eV, assigned to $Au4f_{7/2}$ and $Au4f_{5/2}$, respectively, are in good agreement with the reported values of Au(0), suggesting that the Au species is present in the metallic state[33]. However the peak of Au ($4f_{7/2}$) lower shifted a little relative to that of free metallic Au(0) (~83.8 eV). This difference indicates significant charge transfer from TiO_2 to Au and thus confirms the strong Au/TiO_2 interaction[24]. A Schottky barrier is created between Au(0) and $MesoTiO_2$. Furthermore, XPS was also used to distinguish the surface change of the $MesoTiO_2$ before and after Au loading. Fig.2c display the XPS spectra of Ti 2p of the $MesoTiO_2$ and $Au/MesoTiO_2$, the binding energies of Ti $2p_{3/2}$ and $Ti2p_{1/2}$ are equal to 458.6 eV and 464.4 eV, respectively, suggesting the presence of Ti(□) species[34]. By comparison, there are no measurable changes on the peak positions for Ti2p in $MesoTiO_2$ before and after Au loading. While the XPS spectra of O1s (Fig.2d) shifts from 529.88 to 529.94 eV after Au NPs deposition, owing to the generation of surface oxygen vacancies [35].

For plasmonic composite photocatalysts of $Au/MesoTiO_2$, several parameters including gold particle size, morphology, amount, and the interfacial contact between Au and titania influence its photocatalytic activity. By adding an appropriate concentration of $HAuCl_4 \cdot 3H_2O$ (see in table 1), the $Au/MesoTiO_2$ photocatalysts with different weight percentages (wt%) of Au on $MesoTiO_2$ were prepared using DP

method. The dominant exposed face of the spindle-shaped nanoporous anatase TiO_2 mesocrystals is {101}, and Au NPs do not change any anatase phase of the $MesoTiO_2$. Therefore, the dominant interfacial contact was happened between Au nanoparticles and {101} phase for all samples. Thus, the Au amount has a significant influence on the photocatalytic activity in this study.

Table 1: Physicochemical Properties of Pure $MesoTiO_2$, P25, $Au_{3.0}$/P25 and Au_x/$MesoTiO_2$ with Different Au Contents.

Sample	C($HAuCl_4 \cdot 3H_2O$)(mM)	Phase[a]	$S_{BET}(m^2/g)$[b]	D_p(nm)[c]
$MesoTiO_2$	0	A	73.7	6.9
$Au_{1.0}$/ $MesoTiO_2$	0.51	A	51.8	6.8
$Au_{3.0}$/ $MesoTiO_2$	1.57	A	50.3	7.0
$Au_{5.0}$/ $MesoTiO_2$	2.67	A	68.3	7.2
$Au_{7.6}$/ $MesoTiO_2$	4.19	A	59.2	7.3
P25	0	A and R	57	/
$Au_{3.0}$/P25	1.57	A and R	54	7.5

[a] A: anatase, R: rutile. [b] BET surface. [c]pore diameter

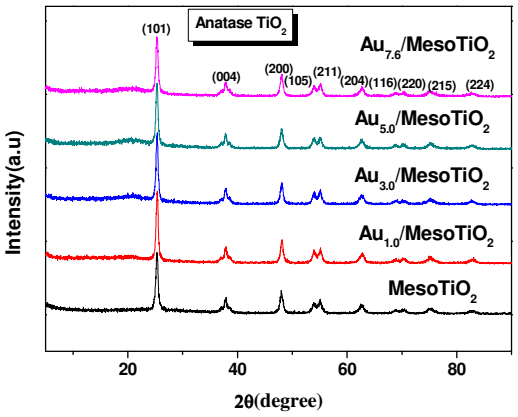

Fig.3XRD patterns of $MesoTiO_2$ and Au/$MesoTiO_2$with various Au loadings.

XRD was used to identify the phase structures of the synthesized samples. Fig.3 shows the X-ray diffraction patterns of pure $MesoTiO_2$ and Au/$MesoTiO_2$, in which all diffraction peaks of the calcined materials (with or without gold incorporation) can

be indexed as anatase TiO_2 with standard values in agreement with that of JCPDS card No. 21-1272. The weird thing is that there is no crystalline Au diffraction peaks observed in all Au/Mes$oTiO_2$ composites. This may be ascribed to the fact that the gold is highly dispersed in the Mes$oTiO_2$ porous structures and the low loading quantity of Au is beyond the XRD detection limit[36]. It should be noted that the formation of single crystalline phase Au through this method is available.

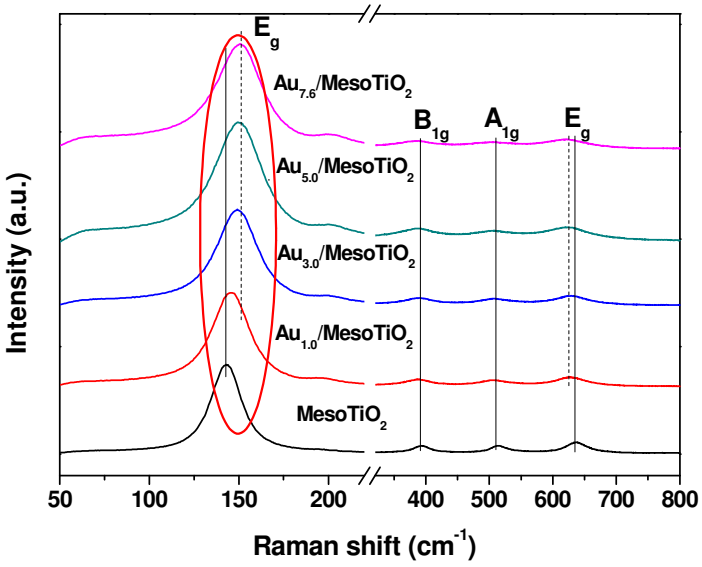

Fig.4 Raman spectra of Mes$oTiO_2$ and Au/Mes$oTiO_2$ with various Au loadings.

To further identify the phases and the crystalline of the samples, Raman studies were performed in the range of 100-1000cm^{-1} that is shown in Fig.4. The Raman peaks at 143.3, 394, 513, 636 cm^{-1} could be assigned to the Raman-active modes of anatase with symmetries E_g, B_{1g}, A_{1g}, and E_g, respectively[37]. Interesting observations were that the E_g peak at 143.3 cm-1 gradually shifted to a higher wavenumber as the Au content increased, however, the E_g peak at 636 cm-1 shifted to the opposite direction. This indicates that there was an interaction between the Au and Mes$oTiO_2$ and the created crystalline defects within the Mes$oTiO_2$ increase with the enhancement of Au content[38]. The crystalline defects affect the characteristic vibrational frequency of the anatase TiO_2, it can act as traps to capture photoelectrons, which make a contribution to inhibiting the charge recombination. Thus, the XRD and Raman characterization of

MesoTiO$_2$ and Au/MesoTiO$_2$ demonstrate the high crystallinity of titania materials and the presence of anatase phase.

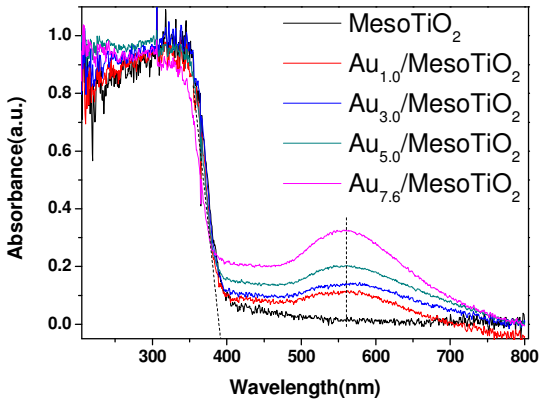

Fig.5 UV-vis absorption spectra of MesoTiO$_2$ and Au/MesoTiO$_2$ with various Au loadings.

Light absorption properties were studied by UV-vis spectroscopy and the effect of Au loading content on UV-vis absorption property are revealed in Fig.5. it shows that the absorption of blank MesoTiO$_2$ is only located at the ultraviolet (UV) region below 370 nm, whereas the Au/MesoTiO$_2$ show two absorption band with the largest absorption edge located near 370nm and the second near 558nm. The presence of two absorption band indicates two step transitions in the band gap. The pronounced low-energy absorption band at 558 nm is in good agreement with the reported values of Au nanoparticles and may be ascribed to the typical surface plasmon resonance (SPR) of Au NPs[25, 39, 40].

It is clear that with the increase of Au content from 1.0wt% to 7.6 wt%, the plasmon band intensity of Au/MesoTiO$_2$ increased accordingly while the light absorption feature of Au/MesoTiO$_2$ in the UV region is the same as that of blank MesoTiO$_2$. The results of UV-vis spectroscopy indicate that Au/MesoTiO$_2$ have the significantly enhanced visible light absorption and they are able to be photoexcited by visible light irradiation, by which electron–hole pairs can be generated and two step-transition guarantee the prolonged electron–hole pairs separation lifetime, thus the improved photoexcited performance can be expected.

We know the peak position and shape of the SPR absorption band are sensitive to the Au particle size and morphology[41]. In Fig.5, no red-shifting phenomenon is occurred, suggesting all Au/MesoTiO$_2$ catalysts have similar Au NPs size (8nm).

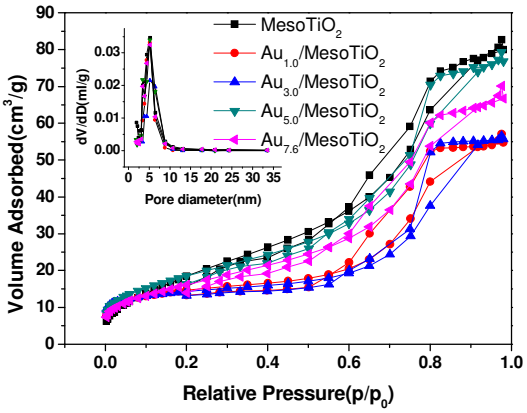

Fig.6 N_2 adsorption-desorption isotherms and pore diameter distribution (inset) of the undopedMesoTiO$_2$ and the Au/MesoTiO$_2$ nanocomposites at 77 K.

The Brunauer-Emmett-Teller (BET) specific surface area (S_{BET}) and pore structure of the MesoTiO$_2$ and Au/MesoTiO$_2$ composites were investigated using N_2 adsorption-desorption measurements at 77 K. All samples exhibit a characteristic type IV isotherm behavior with H2 hysteresis in the Fig.6, corresponding to mesoporous materials with *ink-bottle* structure. The pore distributions of all samples are shown in the inset of Fig.6. All samples display similar narrow pore-size distributions centered at about 4.0~6.0 nm. Detailed surface area and pore structure information are listed in Table 1. Usually, the bigger surface area of photocatalysts, the more promote organic pollutants adsorption, which will result in the difference on final photodegradation efficiency.

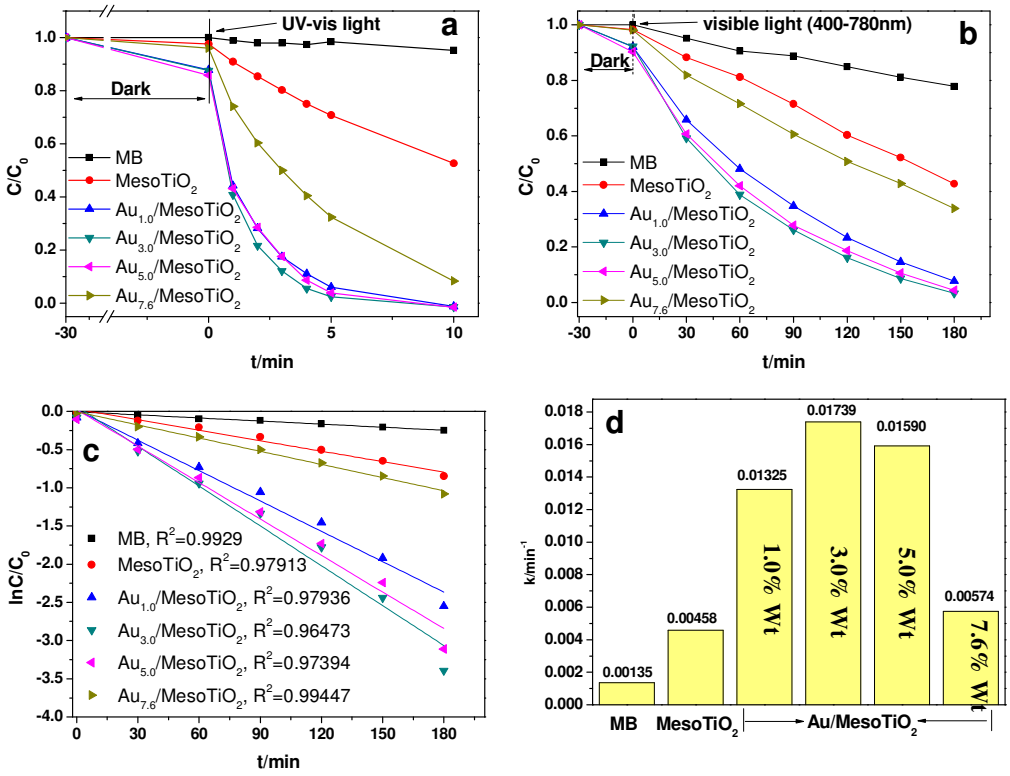

Fig.7 Photodegradation of MB over various samples upon UV-visible light irradiation (a) and visible light irradiation (b). Kinetic linear fitting curves for liquid-phase photocatalytic degradation of MB over different samples under visible light irradiation(c).Value of the rate constant k of the photodegradation of MB over $MesoTiO_2$ and $Au/MesoTiO_2$ composites(d).

The photocatalytic degradation of MB in aqueous phase was selected as the probe reaction to evaluate the photocatalytic activity of $MesoTiO_2$ before and after Au loading. The change of methylene blue concentration as a function of illumination time was shown in Fig.7a and 7b. Under simultaneous UV and visible light irradiation, only 46% degradation was observed over $MesoTiO_2$ within 10 minutes shown in Fig.7a. Whereas, the $Au/MesoTiO_2$ with different Au content demonstrated higher photodegradation efficiency, completely degraded MB within 10 minutes. Through careful observation, the MB degradation efficiency continuously increases with Au loading content increasing from 1 to 3 wt% in the early 5 minutes. Further increasing

Au content, however, decreases catalytic activity. The same rule were observed upon visible light irradiation (400~780nm), but the irradiation time needs 3 hours to quantitive degradation. Among all these visible light photocatalysts, the highest activity has been noticed for $Au_{3.0}/MesoTiO_2$ which degradation efficiency of MB near to 100%. On the basis of a simplified Langmuir-Hinshelwood model, the linear relationship of $\ln(C/C_0)$ versus time (see in Fig.7c) upon visible light irradiation indicates that MB degradation follows a pseudo first order kinetic, and the apparent rate constant (k) shown in Fig.7d was calculated from the plot of $\ln (C/C_0)$ vs time. The highest apparent rate constant, obtained for $Au_{3.0}/MesoTiO_2$, is 1.739×10^{-2} min, which shows a 3.80, 1.31, 1.09 and 3.03-fold photocatalytic activity improvement over $MesoTiO_2$, $Au_{1.0}/MesoTiO_2$, $Au_{5.0}/MesoTiO_2$ and $Au_{7.6}/MesoTiO_2$, respectively.

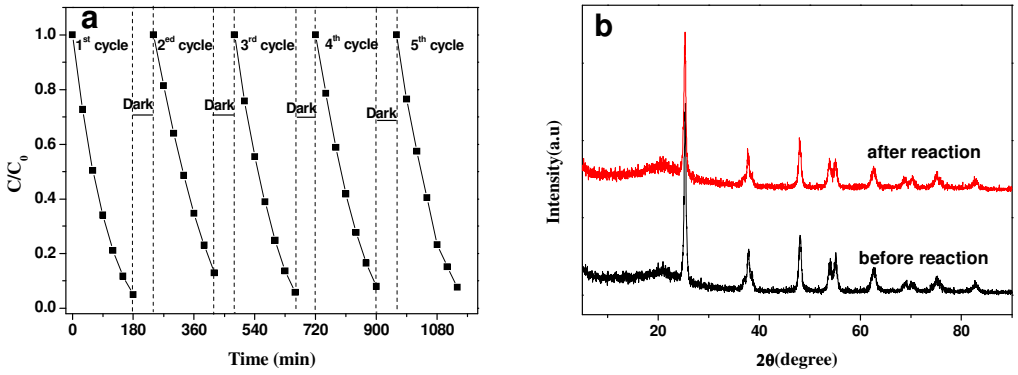

Fig.8 Durability study over $Au_{3.0}/MesoTiO_2$ for MB photodegradation under visible light irradiation (a), XRD patterns of $Au_{3.0}/MesoTiO_2$ after recycling reaction.

Durability test was performed to confirm the stability of the highest result performed by $Au_{3.0}/MesoTiO_2$ photocatalyst, which was very important for the practical application. According to Fig.8a, the MB photodegradation efficiency changed a little after 5 cycles of experiment under identical conditions, indicating that the photocatalyst has superior photocatalytic stability. Moreover, the crystallization was well maintained after recycling test comparing to that of $Au_{3.0}/MesoTiO_2$ before reaction, which was confirmed by Fig.8b. This can be attributed to synergistic effect of the high intrinsic single-crystal-like nature of the anatase phase, the stability of the

gold as well as the strong interaction between the Au and MesoTiO$_2$.

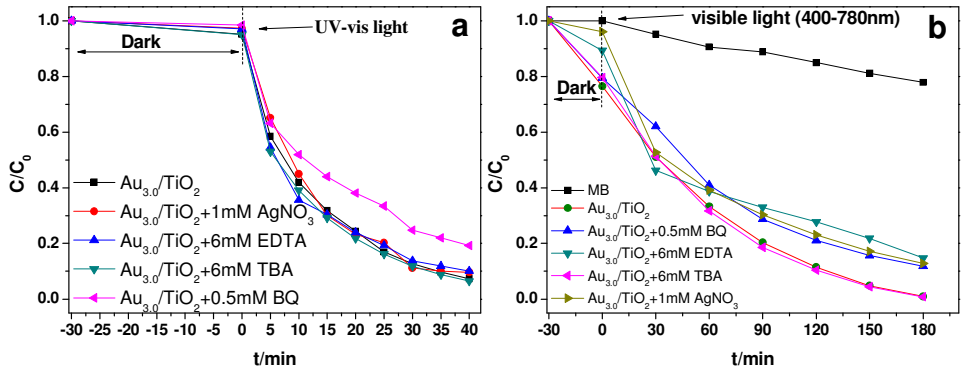

Fig.9 Reaction process for photocatalytic degradation of MB on Au$_{3.0}$/MesoTiO$_2$ catalyst with and without trapping agents. (a) under UV-visible light irradiation, (b) under visible light irradiation.

To investigate the main active species during the photodegradation process, additional examination was carried out via dissolving different trapping agents in the reaction solution before light irradiations. Under UV-visible light irradiation shown in Fig.9a, the MB degradation was significantly suppressed when benzoquinone (BQ), a scavenger for $\cdot O_2^-$ radicals, was added to the reaction system[42]. However, other radical scavengers presented no influence on photoactivity. This indicated that the $\cdot O_2^-$ radical was the main active species during the photodegradation process. It is interesting to note that, under visible light irradiation, the result is different as is shown in Fig.9b. Trapping photo-generated holes and electrons with EDTA and $AgNO_3$, respectively, the degradation rate exhibited moderate suppression. In analogy, when BQ was added to the reaction system, a weaker decrease of degradation rate was also observed, indicating that $\cdot O_2^-$ radical was not the only active species in this condition. Regardless of the kind of light excitation, no significant changes occurred on dye degradation when $\cdot$OH scavengers, TBA, was put into the degradation systems[43]. Accordingly, the possible reaction process can be proposed as follows. The Mechanism for the Photocatalytic activity of Au/MesoTiO$_2$ under UV light excitation

and visible light excitation are different. As is demonstrated from XPS that Au and MesoTiO$_2$ forms a Schottky junction and the metal Au acts as the anode, and n-type MesoTiO$_2$ acts as the cathode. Under simultaneous UV and visible light irradiation (Scheme 1 left part), electrons of TiO$_2$ are rapidly promoted from the valence band (VB) to the conduction band (CB), while holes remain in VB (eq 1). It is easy to transfer electrons from CB to metallic Au through a Schottky junction (eq 2), which extends the lifetime of electron. Then, the electrons reduce O_2 adsorbed on the Au surface to form $\cdot O_2^-$ and further generate $\cdot HO_2$ (eq 3 and 4). Finally, MB molecules adsorbed on the Au surface are oxidized by $\cdot O_2^-$ and $\cdot HO_2$ together. Meanwhile, the hole can initiate the direct oxidation of MB molecules (eq 5).

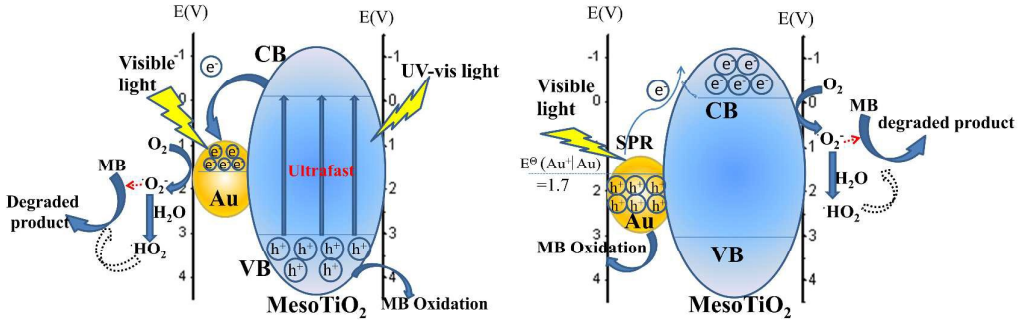

Scheme 1 Proposed mechanism for the photocatalytic activity of Au/MesoTiO2 under UV light excitation (left) and upon excitation of the gold surface plasmon band (right)

$$MesoTiO_2 + h\nu(\geq Eg) \rightarrow MesoTiO_2(e_{cb}^- + h_{vb}^+) \quad (1)$$

$$MesoTiO_2(e_{cb}^-) + Au \rightarrow MesoTiO_2\text{-}Au(e^-) \quad (2)$$

$$MesoTiO_2\text{-}Au(e^-) + O_2 \rightarrow MesoTiO_2\text{-}Au + \cdot O_2^- \quad (3)$$

$$\cdot O_2^- + H_2O \rightarrow \cdot HO_2 + OH^- \quad (4)$$

$$h^+, \cdot O_2^- \text{ or } \cdot HO_2 + MB \rightarrow \text{degraded product} \quad (5)$$

Under visible light irradiation, MesoTiO$_2$ exhibited low photocatalytic ability due to its slight absorption "tail" (Fig.5). Once Au NPs are incorporated into MesoTiO$_2$, upon visible light irradiation as is shown in Scheme 1 right part, intense SPR-enhanced EM fields and resonant photon scattering are generated on the Au NP surface, significantly increasing the yield of interfacial "hot electrons" with a higher potential energy than Schottky barrier height at the interface (eq 6)[44], and the position of the Fermi level will be shifted closer to the CB of MesoTiO$_2$[45]. Subsequently, the

"hot electrons" are transferred to the CB of MesoTiO$_2$ (eq 7). The Schottky barrier at the interface also helps the transferred "hot" electrons accumulate in the TiO$_2$ CB, preventing them from traveling back to the Au NPs. Since no holes are generated in the valence band (VB) of TiO$_2$, the transferred "hot electrons" in the TiO$_2$ CB should have much longer lifetimes, offering more probability to reduce the O$_2$ adsorbed on the MesoTiO$_2$ surface and the consequent sequence MB degradation.

It is known that the reduction potential of electrons scavengers Ag^+ (+0.80V vs NHE at pH 7) is much higher than the TiO$_2$ CB minimum (-0.1V) while lower than the Au^+(+1.70V). Thus, the Ag^+ can easily be reduced by the transferred electrons within TiO$_2$ CB minimum while cannot be reduced by the electrons on Au. That is what we observed in experimental phenomena that the MB degradation was not suppressed by the addition of electrons scavengers in UV-Vis light irradiation while suppressed in visible light irradiation. Under visible light irradiation the h^+ leave behind on Au make it very easy to be chelated by EDTA, which is consistent with the experimental phenomena shown in Fig.9b that the MB degradation was obviously suppressed by the addition of EDTA. The process of photoreaction is very quick[46] and $\cdot O_2^-$ radicals, e^- and h^+ are simultaneously responsible for the photodegradation of MB in visible light irradiation. Obviously, when the competition occurs mentioned above, the h^+ will mainly take the charge of the oxidation of MB molecules (400-780 nm).

$$Au + h\nu(\geq Eg) \rightarrow Au(e^- + h^+) \quad (6)$$

$$Au(e^-) + MesoTiO_2 \rightarrow Au\text{-}MesoTiO_2(e_{cb}^-) \quad (7)$$

4. Conclusion

In summary, Gold Nanoparticle incorporation into nanoporous anatase TiO$_2$ Mesocrystal, denoted as Au/MesoTiO$_2$, were synthesis to modify the photoresponse properties of TiO$_2$ particles and improve its photocatalytic stability. The exposed active {101} facets coupled with the loaded Au nanoparticles dramatically enhanced the visible light photocatalytic performance of the TiO$_2$. SEM and TEM confirmed the as prepared TiO$_2$ spindle-shaped nanoporous mesocrystals structure and the dominant exposed face is {101} facets, the loaded Au NPs are nearly spherical with

an average size of about 8 nm. XPS results confirmed that the deposited Au NPs were metallic Au(0). UV-vis spectroscopy shows that with the increase of Au content, the plasmon band intensity of Au/MesoTiO_2 increased accordingly. BET demonstrates the Au/MesoTiO_2 owns mesoporous materials with *ink-bottle* structure. The prepared Au/MesoTiO2 catalyst is expected to be potential applications in photocatalysis degradation, photocatalytic water splitting, solar cells and sensors etc.. The finding of our work provides a new way to steadily improve photocatalytic efficiency through loading of stable noble metals on the single-crystal-like MesoTiO_2.

Acknowledgements

This work was supported by grants from National Natural Science Foundation of China (No.21473161 and 21271155), Zhejiang Provincial Top Key Academic Discipline of Chemical Engineering and Technology, Alexander von Humboldt Foundation, and Zhejiang SCI-TECH University for 521 distinguished scholar's scheme.

References

1. A. Paracchino, V. Laporte, K. Sivula, M. Graetzel and E. Thimsen, *Nature Materials*, 2011, **10**, 456-461.
2. Q. Xiang, J. Yu and M. Jaroniec, *Journal of the American Chemical Society*, 2012, **134**, 6575-6578.
3. M. R. Hoffmann, S. T. Martin, W. Y. Choi and D. W. Bahnemann, *Chemical Reviews*, 1995, **95**, 69-96.
4. H. Xu, S. Ouyang, L. Liu, P. Reunchan, N. Umezawa and J. Ye, *Journal of Materials Chemistry A*, 2014, **2**, 12642-12661.
5. J. Zhao, L. Zhang, W. Xing and K. Lu, *Journal of Physical Chemistry C*, 2015, **119**, 7732-7737.
6. N. Feng, Q. Wang, A. Zheng, Z. Zhang, J. Fan, S.-B. Liu, J.-P. Amoureux and F. Deng, *Journal of the American Chemical Society*, 2013, **135**, 1607-1616.
7. D. Yang, Y. Sun, Z. Tong, Y. Tian, Y. Li and Z. Jiang, *Journal of Physical Chemistry C*, 2015, **119**, 5827-5835.
8. M.-Y. Xing, B.-X. Yang, H. Yu, B.-Z. Tian, S. Bagwasi, J.-L. Zhang and X.-Q. Gongs, *Journal of Physical Chemistry Letters*, 2013, **4**, 3910-3917.
9. A. A. Ismail, D. W. Bahnemann, I. Bannat and M. Wark, *Journal of Physical Chemistry C*, 2009, **113**, 7429-7435.
10. H. Wang, Y. Fu, T. Han, J. Wan and X. Zheng, *Rsc Advances*, 2015, **5**, 33570-33578.
11. H. Wang, D. Zhou, Z. Wu, J. Wan, X. Zheng, L. Yu and D. L. Phillips, *Materials Research Bulletin*, 2014, **57**, 311-319.
12. H. Wang, D. Zhou, S. Shen, J. Wan, X. Zheng, L. Yu and D. L. Phillips, *Rsc Advances*, 2014, **4**, 28978-28986.
13. L. Liu, X. Gu, C. Sun, H. Li, Y. Deng, F. Gao and L. Dong, *Nanoscale*, 2012, **4**, 6351-6359.
14. H. Tada, Q. Jin, H. Nishijima, H. Yamamoto, M. Fujishima, S.-i. Okuoka, T. Hattori, Y. Sumida and H. Kobayashi, *Angewandte Chemie-International Edition*, 2011, **50**, 3501-3505.
15. T. Han, D. Zhou, H. Wang and X. Zheng, *Journal of Environmental Chemical Engineering*, 2015, **3**, 2453-2462.
16. X. Fu, B. Wang, C. Chen, Z. Ren, C. Fan and Z. Wang, *New Journal of Chemistry*, 2014, **38**, 4754-4759.
17. L. Zhou, D. Smyth-Boyle and P. O'Brien, *Journal of the American Chemical Society*, 2008, **130**, 1309-1320.
18. Z. Bian, T. Tachikawa and T. Majima, *Journal of Physical Chemistry Letters*, 2012, **3**, 1422-1427.
19. Z. Hong, M. Wei, T. Lan, L. Jiang and G. Cao, *Energy & Environmental Science*, 2012, **5**, 5408-5413.
20. C. Hu, X. Zhang, X. Li, Y. Yan, G. Xi, H. Yang and H. Bai, *Chemistry-a European Journal*, 2014, **20**, 13557-13560.
21. L. Liu, P. Li, B. Adisak, S. Ouyang, N. Umezawa, J. Ye, R. Kodiyath, T. Tanabe, G. V. Ramesh, S. Ueda and H. Abe, *Journal of Materials Chemistry A*, 2014, **2**, 9875-9882.
22. L. Liu, S. Ouyang and J. Ye, *Angewandte Chemie-International Edition*, 2013, **52**, 6689-6693.
23. P. Christopher, H. Xin, A. Marimuthu and S. Linic, *Nature Materials*, 2012, **11**, 1044-1050.
24. D. Ding, K. Liu, S. He, C. Gao and Y. Yin, *Nano Letters*, 2014, **14**, 6731-6736.
25. Z. Bian, T. Tachikawa, P. Zhang, M. Fujitsuka and T. Majima, *Journal of the American Chemical Society*, 2014, **136**, 458-465.

26. L. Du, A. Furube, K. Yamamoto, K. Hara, R. Katoh and M. Tachiya, *Journal of Physical Chemistry C*, 2009, **113**, 6454-6462.
27. K. Qian, B. C. Sweeny, A. C. Johnston-Peck, W. Niu, J. O. Graham, J. S. DuChene, J. Qiu, Y.-C. Wang, M. H. Engelhard, D. Su, E. A. Stach and W. D. Wei, *Journal of the American Chemical Society*, 2014, **136**, 9842-9845.
28. M. A. Elmoula, E. Panaitescu, M. Phan, D. Yin, C. Richter, L. H. Lewis and L. Menon, *Journal of Materials Chemistry*, 2009, **19**, 4483-4487.
29. R. Zanella, S. Giorgio, C. R. Henry and C. Louis, *Journal of Physical Chemistry B*, 2002, **106**, 7634-7642.
30. Z. Hong, K. Zhou, J. Zhang, Z. Huang and M. Wei, *Journal of Materials Chemistry A*, 2015, **3**, 17412-17416.
31. J. Ye, W. Liu, J. Cai, S. Chen, X. Zhao, H. Zhou and L. Qi, *Journal of the American Chemical Society*, 2011, **133**, 933-940.
32. F. Chen, F. Cao, H. Li and Z. Bian, *Langmuir*, 2015, **31**, 3494-3499.
33. Y. Wu, J. Zhang, L. Xiao and F. Chen, *Applied Catalysis B-Environmental*, 2009, **88**, 525-532.
34. J. Li and H. C. Zeng, *Chemistry of Materials*, 2006, **18**, 4270-4277.
35. M. Xing, J. Zhang, F. Chen and B. Tian, *Chemical Communications*, 2011, **47**, 4947-4949.
36. H. Wang, J. L. Faria, S. Dong and Y. Chang, *Materials Science and Engineering B-Advanced Functional Solid-State Materials*, 2012, **177**, 913-919.
37. F. Tian, Y. Zhang, J. Zhang and C. Pan, *Journal of Physical Chemistry C*, 2012, **116**, 7515-7519.
38. Y. Li, H. Wang, Q. Feng, G. Zhou and Z.-S. Wang, *Energy & Environmental Science*, 2013, **6**, 2156-2165.
39. A. Ayati, A. Ahmadpour, F. F. Bamoharram, B. Tanhaei, M. Manttari and M. Sillanpaa, *Chemosphere*, 2014, **107**, 163-174.
40. C. Gomes Silva, R. Juarez, T. Marino, R. Molinari and H. Garcia, *Journal of the American Chemical Society*, 2011, **133**, 595-602.
41. K. Takahiro, S.-i. Naya and H. Tada, *Journal of Physical Chemistry C*, 2014, **118**, 26887-26893.
42. Y. Zhang, N. Zhang, Z.-R. Tang and Y.-J. Xu, *Chemical Science*, 2013, **4**, 1820-1824.
43. C. Pan and Y. Zhu, *Environmental Science & Technology*, 2010, **44**, 5570-5574.
44. J. Y. Park, S. M. Kim, H. Lee and B. Naik, *Catalysis Letters*, 2014, **144**, 1996-2004.
45. S. P. Lim, A. Pandikumar, N. M. Huang and H. N. Lim, *Rsc Advances*, 2015, **5**, 44398-44407.
46. K. Ozawa, M. Emori, S. Yamamoto, R. Yukawa, S. Yamamoto, R. Hobara, K. Fujikawa, H. Sakama and I. Matsuda, *Journal of Physical Chemistry Letters*, 2014, **5**, 1953-1957.

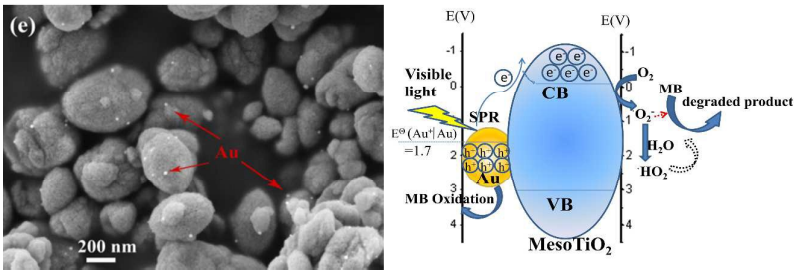

Schottky junction plasmonic photocatalysts were synthesized by the modification of spindle-shaped TiO_2 mesocrystals with Au nanoparticles and the photocatalysis degradation mechanisms are proposed.